

Transformation of polar nematic phases in the presence of electric field

A. V. Emelyanenko^{1,*}, V. Yu. Rudyak¹, F. Araoka², H. Nishikawa², and K. Ishikawa³

¹*Lomonosov Moscow State University, Moscow 119991, Russia*

²*RIKEN Center for Emergent Matter Science (CEMS), 2-1 Hirosawa Wako, Saitama 351-0198 Japan*

³*Tokyo Institute of Technology, 2-12-1 Ookayama, Meguro-ku Tokyo 152-8550 Japan*

Only a few years have passed since discovery of polar nematics, and now they are becoming the most actively studied liquid crystal materials. Despite numerous breakthrough findings made recently, a theoretical systematization is still lacking. In the present paper we are making a step on the way of systematization. A powerful technique that molecular-statistical physics is has been applied to an assembly of polar molecules influenced by electric field. Totally, the three polar nematic phases were found to be stable at various conditions: the double-splay ferroelectric nematic N_F^{2D} (observed in the lower-temperature range in the absence or at low electric field), the double-splay antiferroelectric nematic N_{AF} (observed at intermediate temperature in the absence or at low electric field) and the single-splay ferroelectric nematic N_F^{1D} (observed at moderate electric field at any temperature below transition into paraelectric nematic N and in the higher-temperature range (also below N) at low electric field or without it. A paradoxical transition from N_F^{1D} to N induced by application of higher electric field has been found and explained. A transformation of the structure of polar nematic phases at application of electric field has also been investigated by Monte Carlo simulations and experimentally by observation of POM images. In particular, it has been realized that, at planar anchoring, N_{AF} in the presence of moderate out-of-plane electric field exhibits the twofold splay modulation: antiferroelectric in the plane of the substrate and ferroelectric in the plane normal to the substrate. Several additional sub-transitions related to fitting confined geometry of the cell by the structure of polar phases were detected.

I. INTRODUCTION

One of the main trends in modern science today is the development of new materials, which can be effectively manipulated by electric field for various humans needs, from displays to medicine. Liquid crystals (LCs) fulfill many demands. It was noticed that LCs possessing spontaneous polarization can be better candidates for the novel applications: from fast energy-saving and compact electronics to artificial muscles. However, the layered structures of smectics (the only class of LCs known previously to possess the spontaneous polarization) are poorly resistant to mechanical stress. Over the past few years, several new classes of nematic LCs (which are sustainable to mechanical stress) with unique properties originating from unique symmetry of individual molecules have been discovered.

For the last decades, the formation of spontaneous polarization in the nematic materials has been actively discussed [1–4]. Liquid crystals consisting of bent-core molecules were considered as the main candidates, since they have a significantly (several orders of magnitude) higher flexoelectric coefficient [5]. Indeed, nanosized polar clusters in the nematic phase were found for this kind of mesogens [6]. However, these materials do not possess macroscopic polarization in the absence of external field. Meanwhile, proper ferroelectricity was found in columnar phases composed of umbrella-shaped mesogens [7–9] and in re-entrant smectic phases [10–14].

In 2017, the two scientific groups independently reported about the existence of polar nematic phases in LCs composed of the wedge-shaped molecules [15–17]. In Ref. [18, 19] it was realized that the polar nematic phases can demonstrate spontaneous splay and flexoelectricity, while the existence of splay flexoelectricity in nematic LCs was predicted earlier theoretically in Ref. [20]. It was also noticed in Ref. [21–25] that minor changes in the molecular shape can sufficiently modify the phase sequence.

In Ref. [15] it was demonstrated that DIO material possesses at least three nematic phases: conventional paraelectric nematic phase (N or $M1$) at higher temperature, ferroelectric nematic phase (N_F or MP) at lower temperature and some intermediate phase (N_X or $M2$) in between them. In Refs. [16, 17] and later in Ref. [26] it was confirmed that RM-734 material demonstrates N_F , but does not demonstrate N_X . The anomalously high dielectric permittivity and dielectric anisotropy were found in the N_F phase in both DIO and RM-734 materials [27]. The value of spontaneous polarization in N_F is comparable with that for the solid-state ferroelectrics. At present, many other polar nematic (including chiral and biaxial) phases were found in different materials and mixtures [28–31]. Our theoretical studies

*Electronic address: emel@poly.phys.msu.ru

presented in Ref. [32] suggest that the intermediate $M2$ (or N_X) phase observed in DIO can be the antiferroelectric double splay nematic phase (in correspondence with definition and in complete agreement with Refs. [33, 34]) forming the periodical 2D-splay domains of several micrometers size. The same conclusions follow from dielectric measurements and POM observations in Ref. [15, 35] and measurements of spontaneous polarization and PFM observations in Ref. [26].

Experimentally, it is becoming more and more evident [36] that ferroelectric nematic phase (MP or N_F) also possesses the splay domains. For the uniformity of description, here and below we are going to use the N_F^{1D} and N_F^{2D} notations by combining “ N_F ” with “single-splay” or “double-splay” definitions introduced in Refs. [33, 34]). To be consistent furthermore, we are going to use the N_{AF} notation for $M2$ (N_X), which is antiferroelectric.

There are many expectations about applications of nematic ferroelectrics (NFs). Generally, their behavior at application of electric field is not trivial, in particular, in combination of electric field and surface-related effects [37]. NFs are the good candidates in nonlinear optics [38]. Interesting effects related to the motion of ferroelectric nematic droplets in isotropic melts are considered in Ref. [39], and the light-induced branched structures of NF droplets on the surfaces are observed in Ref. [40]. Various polarization topologies in confined NFs were discussed in Ref. [41].

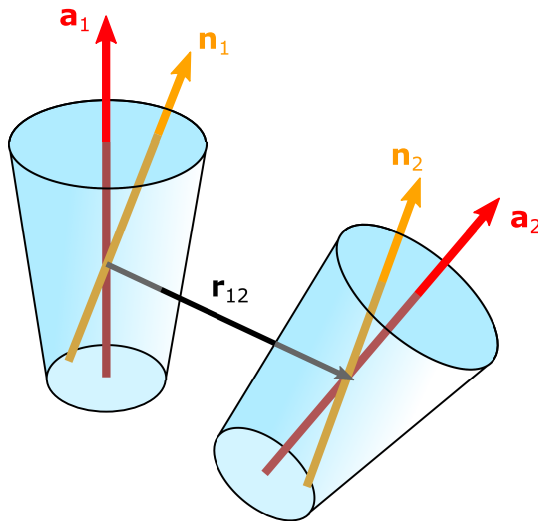


FIG. 1: A pair of interacting polar molecules. Adapted from Ref. [32].

The discussion on how many polar nematic phases can exist, which of them are splayed and which are uniform, which of them are proper and which are improper, is still actual. Recently in Ref. [42] it was reported about the existence of three kinds of NF phases. In the present paper we justify the existence of three (macroscopically uniaxial and achiral) polar nematic phases. In particular, we expect that all three polar phases can be observed in DIO material. We are going to present theoretical explanations, why all three polar phases are splayed and improper ferroelectric. At the same time, since the splay domain size can achieve several micrometers, in some temperature ranges, the splay director deformation can be suppressed by the surfaces if the cell thickness is lower than the domain size.

The paper is organized as follows. In Sec. II the structures of polar nematic phases merged from theory, computer simulations and experiment will be outlined and systemized. In Sec. III the transformations of polar nematic phases induced by variation of temperature and electric field will be investigated. In Sec. IV the theoretical approaches used for analysis of the structures of polar nematic phases will be presented. Finally, in Sec. V the conclusions will be made.

II. THE STRUCTURES OF POLAR NEMATIC PHASES MERGED FROM THEORY, COMPUTER SIMULATIONS AND EXPERIMENT

A. Generalization of elastic free energy for the presence of flexoelectric and induced polarizations

It is known that flexoelectric effect is crucial for the formation of various polar nematic phases. We are considering the polar molecules similarly to that presented in Ref. [32]. Technically, the flexoelectric term in the free energy can be obtained from consideration of specific symmetry of the pair molecular potential. In particular, the effective pair

molecular interaction potential $U_{12}^{ef}(\mathbf{a}_1, \mathbf{a}_2, \mathbf{r}_{12})$ can be approximated by spherical invariants $T_{\ell L \lambda}(\mathbf{a}_1, \mathbf{u}_{12}, \mathbf{a}_2)$, where \mathbf{a}_1 and \mathbf{a}_2 are the principal axes of molecules 1 and 2 located at points \mathbf{r}_1 and \mathbf{r}_2 , respectively, and $\mathbf{u}_{12} \equiv \mathbf{r}_{12}/|\mathbf{r}_{12}|$ is the unit intermolecular vector, $\mathbf{r}_{12} \equiv \mathbf{r}_2 - \mathbf{r}_1$ (Fig. 1):

$$U_{12}^{ef}(\mathbf{a}_1, \mathbf{a}_2, \mathbf{r}_{12}) = - \sum_{\ell, L, \lambda} J_{\ell L \lambda}(r_{12}) T_{\ell L \lambda}(\mathbf{a}_1, \mathbf{u}_{12}, \mathbf{a}_2) \quad . \quad (1)$$

Introducing the polar $P(\mathbf{r})$ and non-polar $S(\mathbf{r})$ orientational order parameters

$$P(\mathbf{r}) \equiv \int f[(\mathbf{a} \cdot \mathbf{n}), \mathbf{r}] P_1(\mathbf{a} \cdot \mathbf{n}) d^2 \mathbf{a} \quad , \quad S(\mathbf{r}) \equiv \int f[(\mathbf{a} \cdot \mathbf{n}), \mathbf{r}] P_2(\mathbf{a} \cdot \mathbf{n}) d^2 \mathbf{a} \quad , \quad (2)$$

where $f[(\mathbf{a} \cdot \mathbf{n}), \mathbf{r}]$ is the orientational distribution function for molecules having principal axes \mathbf{a} with respect to

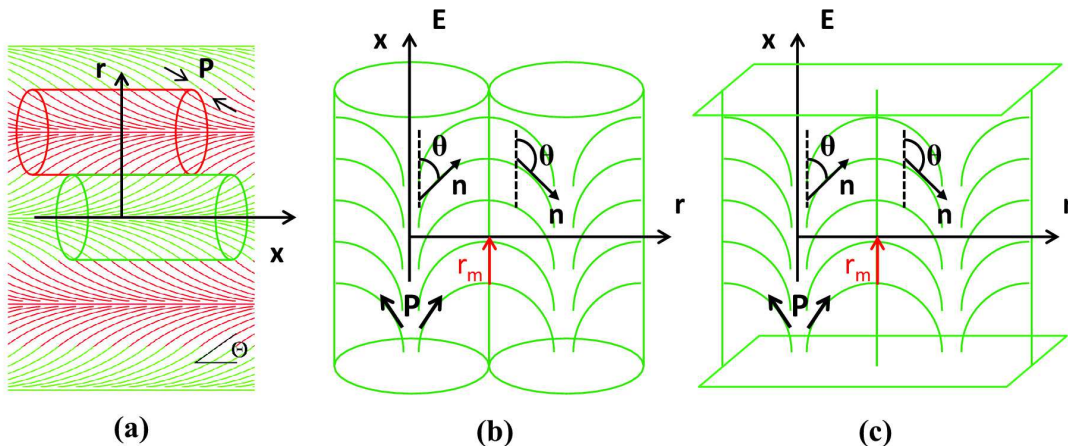


FIG. 2: Director distribution in N_{AF} (a), N_F^{2D} (b) and N_F^{1D} (c). Green color corresponds to the positive splay and polarization, red color corresponds to the negative splay and polarization; \mathbf{x} -axis is either along the domain symmetry axis in (a) and (b) or along the symmetry plane in (c); \mathbf{r} -axis is perpendicular to \mathbf{x} -axis; θ is the angle between the local director \mathbf{n} and \mathbf{x} -axis; \mathbf{P} is the local polarization.

director \mathbf{n} at point \mathbf{r} , and using the gradient expansion of the director [43, 44], we obtain the flexoelectric term as the average of $T_{110}(\mathbf{a}_1, \mathbf{u}_{12}, \mathbf{a}_2)$ and $T_{011}(\mathbf{a}_1, \mathbf{u}_{12}, \mathbf{a}_2)$ polar invariants [32]:

$$\langle J_{110}(r_{12}) T_{110}(\mathbf{a}_1, \mathbf{u}_{12}, \mathbf{a}_2) + J_{011}(r_{12}) T_{011}(\mathbf{a}_1, \mathbf{u}_{12}, \mathbf{a}_2) \rangle \implies \lambda P(\nabla \cdot \mathbf{n}) \quad , \quad (3)$$

where λ is proportional to flexoelectric coefficient. The elastic free-energy density can be generalized by inclusion of flexoelectric splay term and the term related to the presence of external electric field:

$$\frac{\partial F_{\mathbf{n}}}{\partial V} = \frac{1}{2} K_{11} \{ \mathbf{n}(\nabla \cdot \mathbf{n}) - \lambda \mathbf{P} \}^2 + \frac{1}{2} K_{22} (\mathbf{n} \cdot [\nabla \times \mathbf{n}])^2 + \frac{1}{2} K_{33} [\mathbf{n} \times [\nabla \times \mathbf{n}]]^2 - \varepsilon_a (\mathbf{E} \cdot \mathbf{P}) \quad , \quad (4)$$

where $\mathbf{P}(\mathbf{r})$ is the vector having absolute value $P(\mathbf{r})$ [see definition in Eq. (2)] and (at positive P) parallel to particular direction (one of the two opposite directions) of pseudovector $\mathbf{n}(\mathbf{r})$, K_{11} , K_{22} and K_{33} are the splay, twist and bend elastic constants, respectively, $K_{11}\lambda$ is the flexoelectric constant [Eq. (3)], and ε_a is the dielectric anisotropy of the material. At positive λ , polarization \mathbf{P} is parallel to director \mathbf{n} at positive splay ($\nabla \cdot \mathbf{n}$), and is anti-parallel to \mathbf{n} at negative splay. Here we should note that Eq. (4) is only a part of the free-energy density, which explicitly depends on director \mathbf{n} , but it does not contain all the terms depending on the polarization value P . The total free-energy density will be considered in Sec. IV.

B. Equilibrium structures of polar nematic phases

To obtain the equilibrium structures of polar nematic material at various conditions, we should minimize the total free energy independently with respect to director $\mathbf{n}(\mathbf{r})$ and orientational distribution function $f[(\mathbf{a} \cdot \mathbf{n}), \mathbf{r}]$. The whole director-dependent part of the free-energy density is presented in Eq. (4), while the total free-energy density

depending explicitly on the orientational distribution function $f[(\mathbf{a} \cdot \mathbf{n}), \mathbf{r}]$ will be considered in the framework of molecular statistical theory in Sec. IV A. One notes, however, that Eq. (4) contains also polarization $\mathbf{P}(\mathbf{r})$, which is determined by function $f[(\mathbf{a} \cdot \mathbf{n}), \mathbf{r}]$ in correspondence with Eq. (2), and therefore the director and the orientational distribution function are correlated. This correlation will be considered in the framework of perturbation theory in Sec. IV B. Theoretical part requires, however, some geometrical simplification, such as consideration of the axial

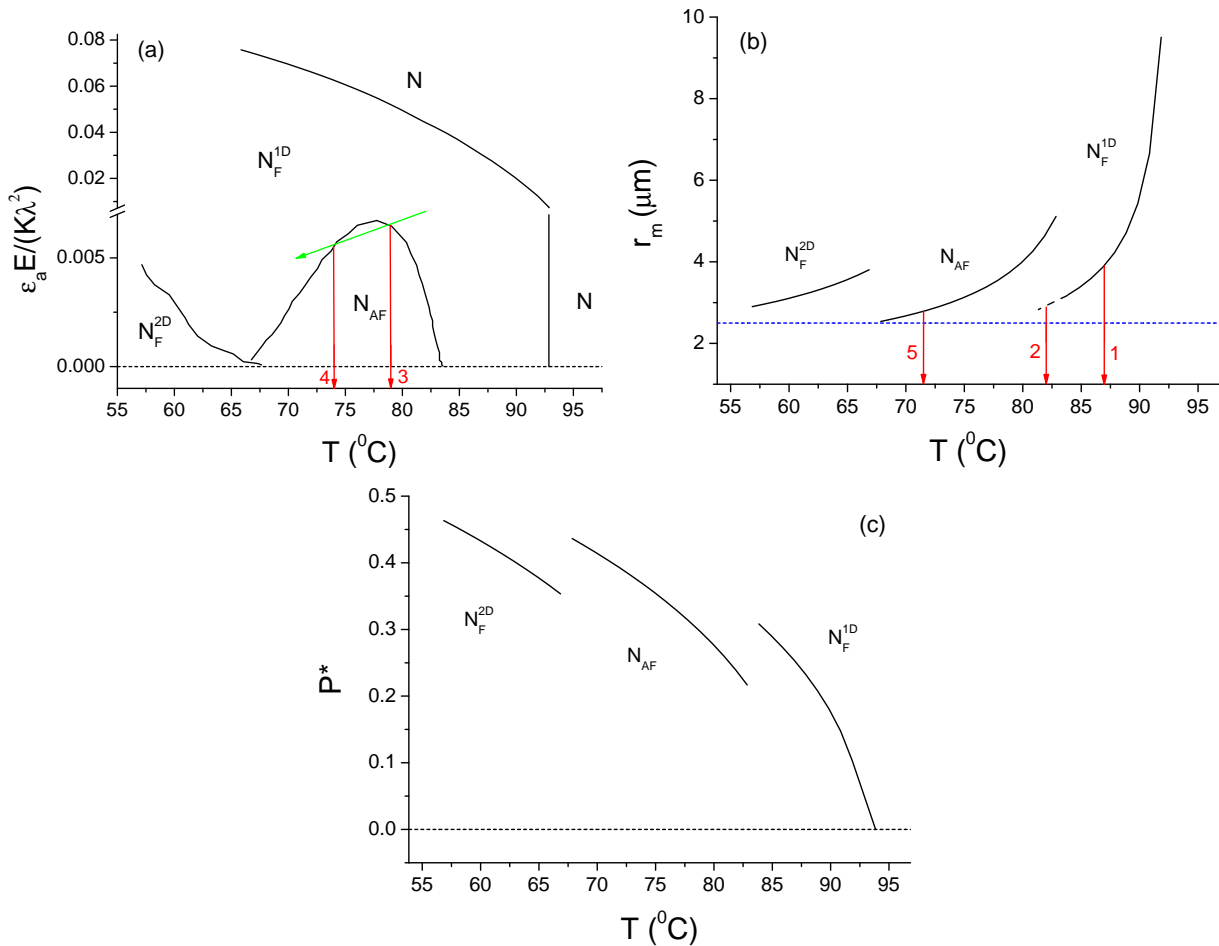


FIG. 3: Electric field – temperature phase diagram (a); Temperature dependencies of the domain radius (b) and characteristic polar order parameter (c) at $E = 0$. Green arrow in (a) tentatively corresponds to the phase sequence with temperature variation at fixed $E \neq 0$. Red arrows with numbers in (a) and (b) correspond to the temperatures of specific phase transitions observed experimentally [Sec. III B]. Dash blue line in (b) corresponds to the half-thickness of the cell.

and planar symmetries. Within these symmetry restrictions, at various conditions we find the three basic structures, which are presented in Fig. 2. At the same time, from computer simulations (Sec. IV C) we can see the more detailed information about the transformations between structures presented in Fig. 2, and the transient structures have obviously more complex geometry. The first basic structure is the double-splay antiferroelectric nematic phase N_{AF} (designated also N_X or $M2$ elsewhere) with alternating signs of the splay and polarization in space. The other two basic structures, stable at different conditions, are the double- and single-splay ferroelectric nematics, N_F^{2D} and N_F^{1D} , respectively. N_F^{2D} and N_{AF} are composed of quasi-cylindrical periodical domains, while N_F^{1D} is composed of planar periodical domains. For each structure presented in Fig. 2, the \mathbf{x} -axis can be introduced, to which the director is parallel in the middle of each domain. In N_F^{2D} and N_{AF} , the director exhibits variation along radius \mathbf{r} of cylinder, while in N_F^{1D} the director exhibits variation along single space direction (for uniformity of equations, also designated as \mathbf{r}). In all cases, \mathbf{r} is perpendicular to \mathbf{x} . In ferroelectric phases, N_F^{2D} and N_F^{1D} , the projection of polarization on the \mathbf{x} -axis does not alternate in sign, while in antiferroelectric N_{AF} , polarization alternates periodically in sign along each Cartesian coordinate.

The electric field – temperature phase diagram is presented in Fig. 3 (a), while the temperature dependencies of the domain radius and characteristic polar order parameter at $E = 0$ are presented in Figs. 3 (b) and (c), respectively.

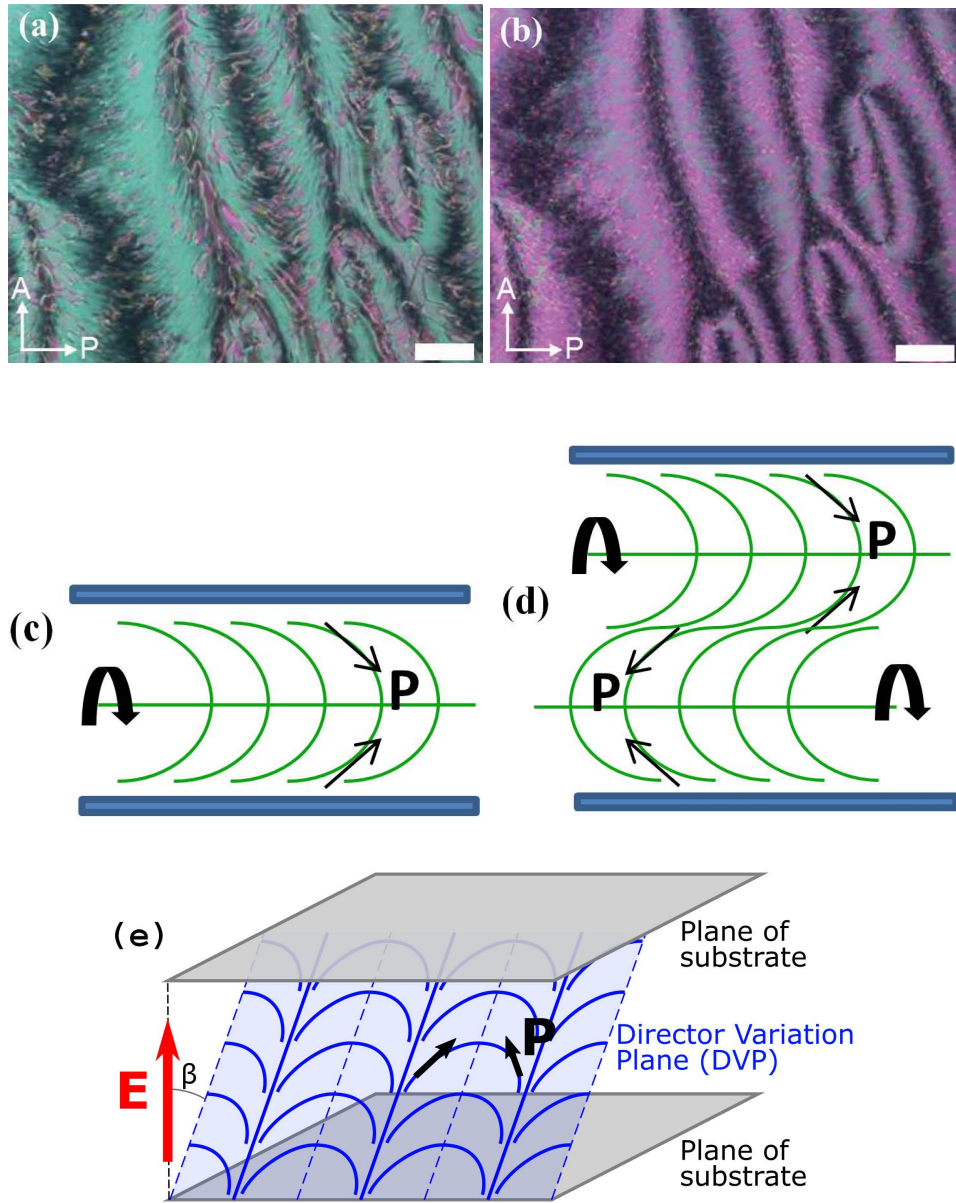


FIG. 4: POM images of quasi-cylindrical domains in N_F^{2D} (a) and N_{AF} (b); orientation of planar domains (schematic illustration) in N_F^{1D} (c) and N_{AF}^{1D} (d) at $E = 0$; orientation of planar domains in N_F^{1D} at $E \neq 0$. In (a) and (b) DIO material is used, cell thickness $10 \mu\text{m}$, scale bar $100 \mu\text{m}$. Images of (a) and (b) are reproduced with permission from Ref. [15]. Copyright WILEY-VCH Verlag GmbH & Co. KGaA, Weinheim, 2017.

From theory (Sec. IV B) it follows that, within each polar phase, the domain radius r_m increases and polarization P^* decreases with the increasing temperature, while multiple $r_m P^*$ remains constant. At zero electric field, N_F^{2D} minimizes the free energy at lower temperature, N_F^{1D} phase minimizes the free energy at higher temperature, and N_{AF} minimizes the free energy in between. The domains in N_F^{2D} and N_{AF} are visible in microscope [see Figs. 4 (a) and (b), respectively], their typical size is several micrometers. In the absence of electric field, the domains in N_F^{1D} at planar anchoring [Fig. 4 (c)] are not visible, because the energy-optimal configuration of the domains makes no optical difference between any points on the glass substrate. In the absence of electric field, the antiferroelectric single-splay phase [Fig. 4 (d)] possesses the same free energy as the ferroelectric one. The plane of each arc in Figs. 4 (c) and (d) can be vertical or tilted. At moderate values of electric field, all the splay nematic phases transform into N_F^{1D} [the orientations of arcs in N_F^{1D} in the presence of moderate electric field are shown in Fig. 4 (e), they can be vertical ($\beta = 0$) or tilted ($\beta \neq 0$) to fit the cell gap] and at higher values of electric field – into paraelectric N having uniform director orientation.

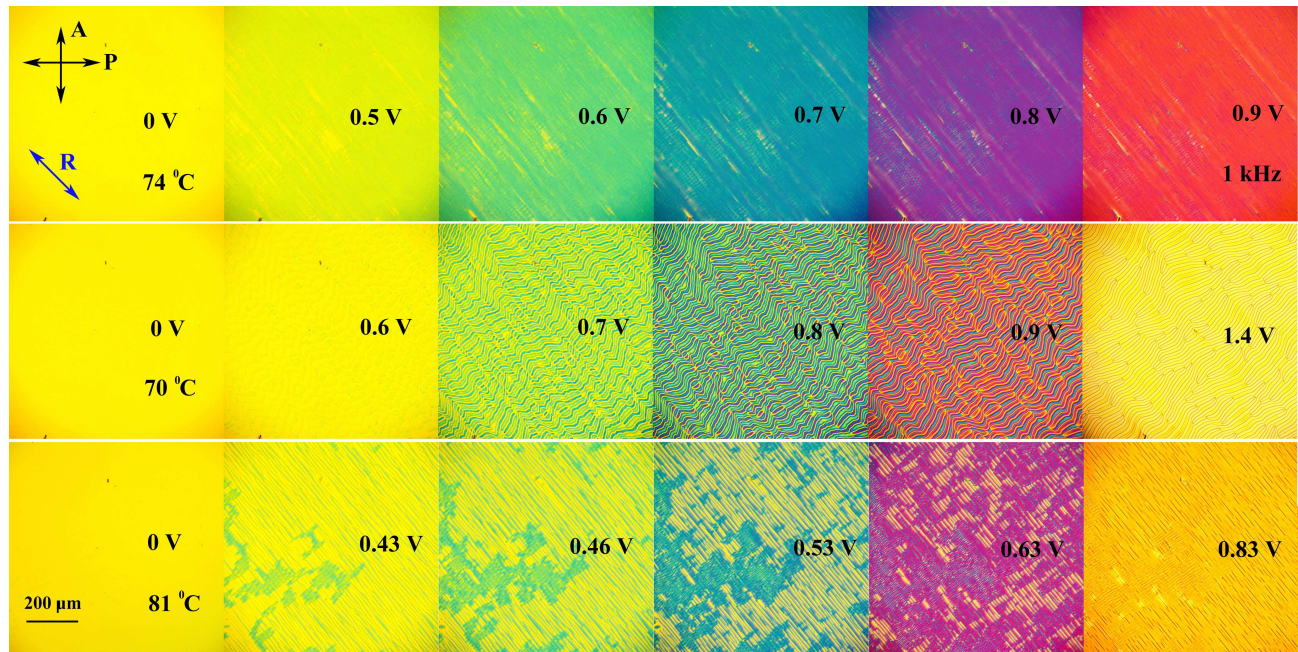


FIG. 5: POM images of the DIO planar cell (cell thickness is $5 \mu m$) at several voltages (sinusoidal signal, $1 kHz$) and temperature $T = 74^\circ C$ (Row 1), $70^\circ C$ (Row 2) and $81^\circ C$ (Row 3). P and A are directions of polarizer and analyzer, R is the rubbing direction.

III. TRANSFORMATIONS OF POLAR NEMATIC PHASES INDUCED BY VARIATION OF TEMPERATURE AND ELECTRIC FIELD

A. Transformation of N_{AF} and N_F^{2D} into N_F^{1D} in electric field

Let us consider the variation of N_{AF} in the electric field, as it seen from POM and computer simulations (Sec. IV C). The $5 \mu m$ -thick planar cell was filled with DIO liquid crystal in isotropic state. After that, the sample was examined by polarizing optical microscope (Nikon V100N Pol, Japan) equipped with a heating stage (TMS-93 Stage Temp Controller and THMS 600 microscope stage, UK). The voltage from a waveform generator (Agilent 33220A, USA) was applied to the ITO-coated cell substrates.

On cooling in the absence of electric field, N_{AF} is observed between $68.8^\circ C$ and $84.5^\circ C$ [15]. The $1 kHz$ frequency electric field of various amplitude was applied at several temperatures within this range. The images of the structure variation at application of electric field are presented in Fig. 5. From computer simulations (Sec. IV C) it follows that the antiferroelectric splay remains in the plane of the substrate and gradually disappears when the voltage increases, while the ferroelectric splay arises in the direction perpendicular to the glass and gradually increases. Starting from particular voltage, the stripes corresponding to the director periodical modulation in space rotate from longitudinal (parallel to the rubbing direction) to transverse (perpendicular to the rubbing direction). In the $5 \mu m$ -thick planar cell, in correspondence with Fig. 3 (b), the domains are bigger than the cell thickness almost in the whole temperature range of N_{AF} and are therefore suppressed at the ground state (at $E = 0$) by the surfaces. From birefringence measurements in Ref. [32] we also conclude that, at $0V$, the conventional paraelectric nematic phase is observed. Temperature $74^\circ C$ (Row 1 in Fig. 5) corresponds to the middle of the temperature range of N_{AF} in the infinite bulk. At $0.6V$ the structure with longitudinal stripes, which is similar to the one obtained in computer simulations, arises. When the voltage increases, one can observe the gradual disappearance of the longitudinal stripes and appearance of the transverse ones. At $70^\circ C$ (Row 2 in Fig. 5) the AF to F transition threshold [Fig. 3 (a)] corresponds to the lower voltage, therefore $0.6V$ is sufficiently large voltage to cross over directly to the ferroelectric state, and only the transverse stripes are observed. One notes, that at each transverse stripe, the middle of each arc presented in Fig. 4 (e) fully satisfies the planar alignment at vertical orientation of director variation plane ($\beta = 0$). When the voltage increases, the director modulation first increases, but at higher voltage starts decreasing again. At $81^\circ C$ (Row 3 in Fig. 5) the situation is generally the same. First, the longitudinal stripes appear, then the transverse ones. Surprisingly, at any temperature, at higher voltage the structure is targeted to become planar paraelectric again. This mainly happens due to disbalance between the induced and flexoelectric polarizations, which is discussed in details

in Sec. IV B.

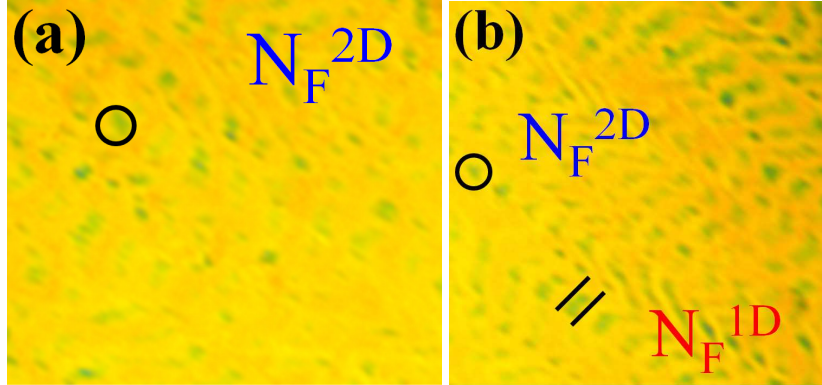


FIG. 6: POM images of the two parts of the cell with DIO at $67^\circ C$ under $0.4V$, $1kHz$ electric field: (a) mostly N_F^{2D} ; (b) transformation from N_F^{2D} to N_F^{1D} .

From experimental observation it also follows that transformation from N_F^{2D} to N_F^{1D} induced by electric field also happens continuously, while all the phase borders presented in Fig. 3 (a) follow from consideration of simplified geometries (either planar or cylindrical) and rather indicate tentative places on the diagram where the continuous transformations between phases should happen. In Fig. 6, a POM images of a planar cell of DIO material at $67^\circ C$ (just below the temperature of transition from N_F^{2D} to N_{AF}) are presented at application of $0.4V$, $1kHz$ electric field. The major part of the cell [Fig. 6 (a)] represents a conjugation of N_F^{2D} cylindrical domains with each other, similar to those presented in Fig. 3 (b). Another part of the cell [Fig. 6 (b)] demonstrates a continuous transformation from N_F^{2D} to N_F^{1D} . The quasi-cylindrical domains continuously transform into the elongated ones and then to the linear stripes. Here the darker dots and lines correspond to $\theta \rightarrow 0$ and π (the places where the director is parallel to electric field – at cylinder axes or in the middle planes of planar domains, see definition of angle θ in Fig. 2). The brighter surrounding corresponds to $\theta \rightarrow \pi/2$ (the places where the director is parallel to the substrate – at the domain periphery). At higher voltage, the whole system transforms into N_F^{1D} and then into paraelectric N .

B. Variation of the structure of DIO on cooling at applied voltage

Let us consider the temperature-induced phase transitions in polar nematic in the presence of electric field. The $5\mu m$ -thick planar cell filled with DIO material was cooling from $99^\circ C$ down to $27^\circ C$ at applied $1kHz$ frequency electric field with constant amplitude $0.9V$. The images in crossed polarizers were registered each half-degree. The phase sequence generally appears to be completely different from that observed without electric field. Particular key images are presented in Figs. 7 and 8. The images practically do not change between $99^\circ C$ and $87^\circ C$ (see Fig. 7). Presumably we observe the uniform paraelectric nematic with planar orientation of director in this temperature range. One notes that our theoretical phase diagram presented in Fig. 3 (a) predicts the existence of the N_F^{1D} polar phase below $93^\circ C$. However, in correspondence with Fig. 3 (b), an equilibrium domain length (corresponding to the infinite bulk of LC) in the temperature range between $93^\circ C$ and $87^\circ C$ is predicted to be huge, and, in realistic confined geometry, the splay domains are most likely suppressed by the substrates. However, below $87^\circ C$ the images start gradually becoming darker, and some longitudinal stripes arise.

The red arrows with numbers presented in Figs. 3 (a) and (b) reflect the temperatures of particular phase transitions observed in DIO at applied fixed voltage, and Arrow 1 tentatively corresponds to the realistic temperature of transition from paraelectric N to N_F^{1D} in DIO confined between parallel glasses ($87^\circ C$). At $87^\circ C$ the equilibrium domain size in N_F^{1D} is still greater than the cell thickness. However, we expect that the highly tilted (almost parallel to the substrate, $\beta \rightarrow \pi/2$) single-splay domains can already exist. The electric field would like to make the director variation plane vertical [perpendicular to the substrates, $\beta = 0$ in Fig. 4 (e)], but in this case the splay domains would not fit the gap between glasses. In this situation, both arms of each arc in Fig. 4 (e) choose the longitudinal (parallel to the rubbing) orientation, and this could be the origin of the longitudinal stripes observed in the temperature range between $87^\circ C$ and $82^\circ C$. When the temperature decreases down to $82^\circ C$, the domain size decreases continuously [see Fig. 3 (b)], therefore the arcs presented in Fig. 4 (e) gain larger and larger vertical projection (which is favorable for the coupling of flexoelectric polarization with electric field), and the images in crossed polarizers are becoming darker and darker.

Surprisingly, the structure variation does not demonstrate any irregular variation near the transition into N_{AF} registered at $84.5^\circ C$ in Ref. [15] by DSC measurements in the absence of electric field, which indirectly indicates

that the structure of LC does not have any tendency to return to the ground state between pulses of high-frequency electric field. An easy explanation for this effect is that the switch-off relaxation time should be much longer than the inverse frequency of electric field in this temperature range. This could be related to the fact that flexoelectric polarization inversion requires the director splay inversion in the whole space. However, the director is trapped by its own periodical structure. The alternative to the director continuous motion is the total director disruption in the whole space, whose energy cost is much higher. Since the director is determined on the scale, which is much larger than molecular size, the director motion is analogous to that of the Brownian particles, whose velocity is much slower than molecular velocity. Our expectation following from Einstein-Smoluchowski equation is that director should not move faster than several micrometers per second, which means that application of $1kHz$ frequency electric field should definitely trap the director distribution within the $5\mu m$ -thick cell, since the director can only move a few nanometers per a pulse. If the frequency of electric field is between the inverse τ_{on} and τ_{off} , the director should stay in the position of particular (let's say, positive) pulse, and should not return to the ground state between pulses. Detailed analysis of all the images of DIO material obtained at application of the high-frequency electric field demonstrates good correlation with our theoretical predictions obtained in a supposition of constant electric field used in Sec. IV.

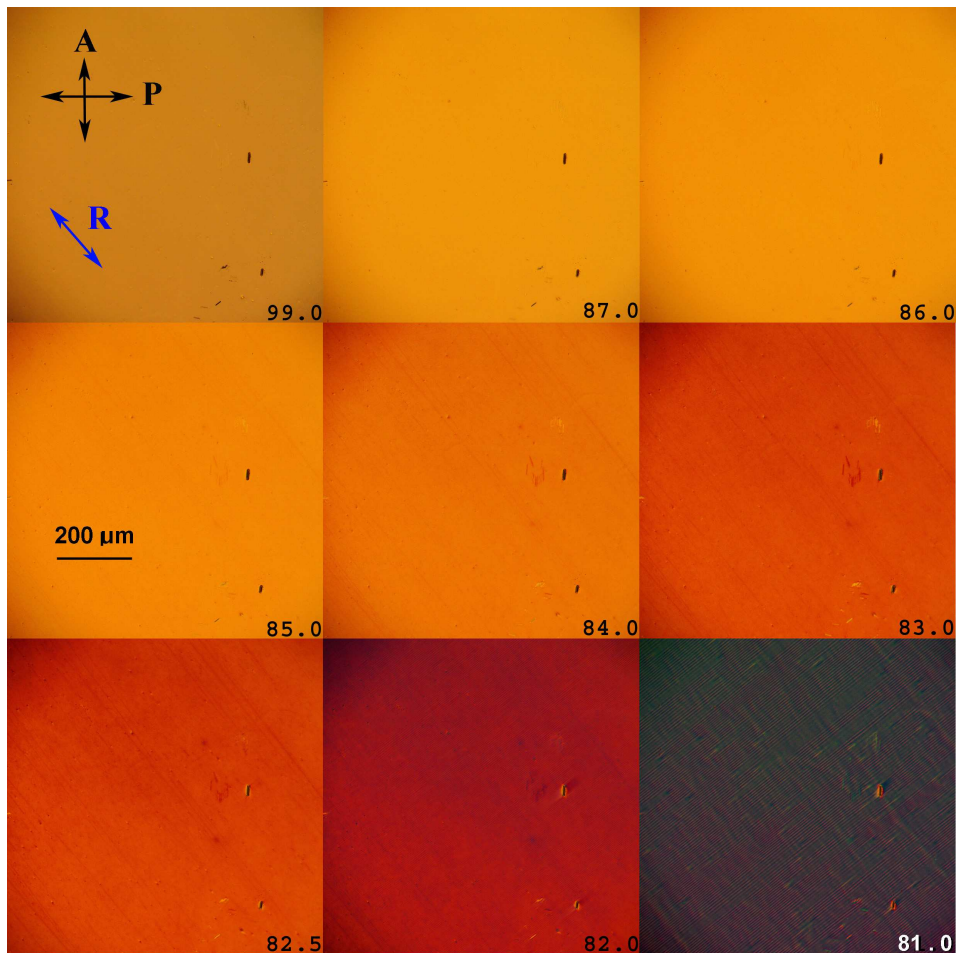


FIG. 7: POM images of the DIO planar cell (cell thickness is $5\mu m$) at applied fixed electric field ($0.9V$, sinusoidal signal, $1kHz$) during the cooling cycle (temperatures are indicated in the bottom right corners). P and A are directions of polarizer and analyzer, R is the rubbing direction.

The next phase transition [marked with Arrow 2 in Fig. 3 (b)] takes place at some temperature between $82^{\circ}C$ and $81^{\circ}C$ (see Fig. 7), at which the transverse (perpendicular to the rubbing direction) stripes appear, and the whole image becomes darker step-wise. This transition is most likely the first-order and is related to the reorientation of director variation plane [reorientation of each arc presented in Fig. 4 (e) around vertical axis]. The reason is that the vertical projection of each arc is already sufficiently great at $82^{\circ}C$, and the middle of each arc is targeted to be oriented along the rubbing direction, while the arms of each arc, on the contrary, are not biased anymore.

From observation of images presented in Fig. 8 it follows, that between $80^{\circ}C$ and $79^{\circ}C$ [Arrow 3 in Fig. 3 (a)] the

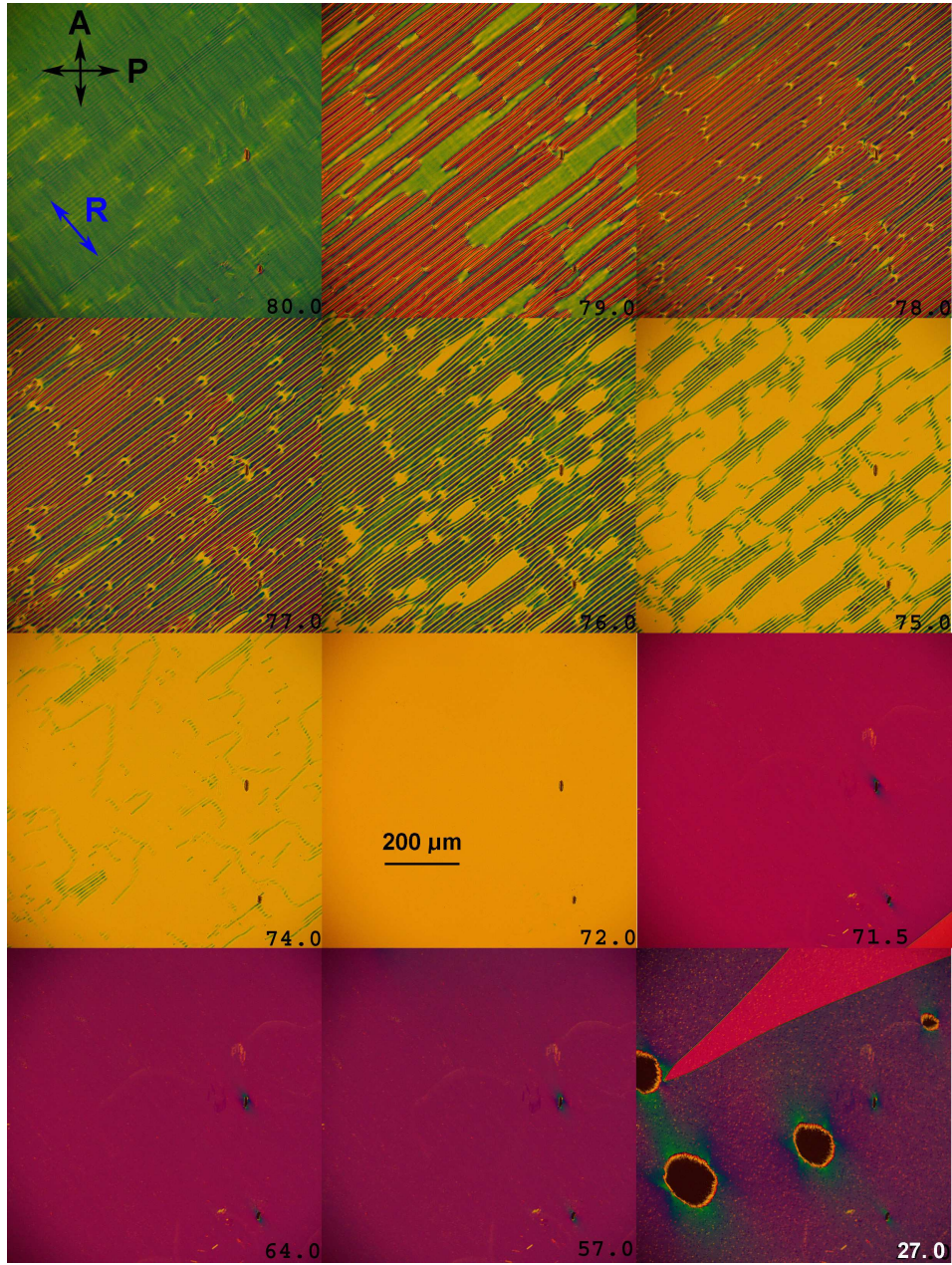


FIG. 8: POM images of the DIO planar cell (cell thickness is $5 \mu m$) at applied fixed electric field ($0.9V$, sinusoidal signal, $1 kHz$) during the cooling cycle (continuation of Fig. 7).

transition from N_F^{1D} to the phase corresponding to N_{AF} deformed in the electric field (see discussion in Sec. III A) takes place. Tentatively, the structure variation in this temperature range follows the green arrow in Fig 3 (a), which is inclined, because the splay elastic constant (participating in the denominator of the value plotted on the vertical axis) should tentatively increase with the decreasing temperature, at least within the range of a single phase. One can see the islands of N_{AF} inside of N_F^{1D} at $80^\circ C$, and therefore the N_F^{1D} to deformed N_{AF} phase transition is also of the first order.

At about $74^\circ C$ the structure comes out of the N_{AF} range [Arrow 4 in Fig. 3 (a)]. Formally, the structure should return to N_F^{1D} . However, it was demonstrated in Sec. III A that, at this temperature and voltage, the director splay modulation is not very deep, and the structure rather resembles the paraelectric nematic with planar director orientation. The origin of this effect will be discussed Sec. IV B.

At $71.5^\circ C$ the new phase transition happens [Arrow 5 in Fig. 3 (b)]. From our observations in Ref. [32] and also from Fig. 3 (b) it follows that the size of domains in N_{AF} becomes comparable to the cell thickness at around $71.5^\circ C$,

and thus, the stripes corresponding to the splay domains in N_{AF} would arise at $E = 0$. Above $71.5^\circ C$ the structures of DIO at applied voltage and in the ground state are the same – the planar paraelectric nematic, while below $71.5^\circ C$ they become different again. The observed structure returns to the one resembling N_F^{1D} observed between $82^\circ C$ and $87^\circ C$ with partial inclusions of the N_F^{2D} domains, whose axes (visible as reflecting dots) are oriented parallel to the electric field and perpendicular to the substrates. When the temperature farther decreases (see Fig. 8), the images become darker, and the number of reflecting dots increases. The structure variation completely ignores the N_{AF} to N_F^{2D} transition registered at $68.8^\circ C$ by DSC measurements in Ref. [15] in the absence of electric field, and thus, the structure does not return to the ground state again, similarly to that in the temperature range between $82^\circ C$ and $87^\circ C$.

At $57^\circ C$ the material structure is already close to the nominal transition into N_F^{2D} . At $27^\circ C$, the structure corresponding to the quasi-ideal N_F^{2D} with islands of crystal and also with some domains similar to those reported in Ref. [45], consideration of which is beyond the scope of the present paper, arises. At different temperatures we observe similar domains at application of much higher voltage, at which we already expect an induction of paraelectric nematic phase by electric field (see discussion in Secs. III A and IV B). One notes that, at planar boundary conditions, in the presence of electric field we obtained an image of N_F^{2D} similar to that obtained at homeotropic boundary conditions without electric field in Ref. [15].

IV. THEORETICAL APPROACHES

A. Molecular-statistical theory: temperature and electric field dependent distributions of S and P order parameters in space

Let us consider a system of elongated polar molecules (with longitudinal electric dipoles $\boldsymbol{\mu}$) interacting with each other and with external electric field \mathbf{E} (Fig. 9). Formally, constant electric field participates in all equations below. Having in mind our discussion in Sec. III B about slow relaxation of director splay, we expect that the structures arising at high-frequency electric field do not differ very much from those obtained at constant electric field. In the general case, director field $\mathbf{n}(\mathbf{r})$ is inhomogeneous, and the free-energy density $\partial F/\partial V$ can be written in the following form Ref. [43]:

$$\begin{aligned} 4\pi V_0 \frac{\partial F(\mathbf{r}_1)}{\partial V} = & k_B T \int d^2 \mathbf{a}_1 f[(\mathbf{a}_1 \cdot \mathbf{n}_1), \mathbf{r}_1] \ln f[(\mathbf{a}_1 \cdot \mathbf{n}_1), \mathbf{r}_1] \\ & + \frac{\sigma_0}{8\pi V_0} \int d^2 \mathbf{a}_1 \int d^2 \mathbf{a}_2 \int d^3 \mathbf{r}_{12} f[(\mathbf{a}_1 \cdot \mathbf{n}_1), \mathbf{r}_1] f[(\mathbf{a}_2 \cdot \mathbf{n}_2), \mathbf{r}_2] U_{12}^{ef}(\mathbf{a}_1, \mathbf{a}_2, \mathbf{r}_{12}) \\ & - 4\pi \mu (\sigma_0 + 1) \int d^2 \mathbf{a}_1 f[(\mathbf{a}_1 \cdot \mathbf{n}_1), \mathbf{r}_1] (\mathbf{a}_1 \cdot \mathbf{E}) \quad , \end{aligned} \quad (5)$$

where V_0 is the bulk occupied by a molecule located at point \mathbf{r}_1 and all its nearest neighbors, σ_0 is the average number of neighbors for each molecule, $f[(\mathbf{a} \cdot \mathbf{n}), \mathbf{r}]$ is the orientational distribution function for molecules having principal axes \mathbf{a} with respect to director \mathbf{n} at point \mathbf{r} , \mathbf{r}_i ($i = 1, 2$) are the coordinates of points 1 and 2, where molecules 1 and 2 are located, \mathbf{r}_{12} is the vector connecting points 1 and 2, k_B is the Boltzmann constant, T is the temperature, $U_{12}^{ef}(\mathbf{a}_1, \mathbf{a}_2, \mathbf{r}_{12})$ is the effective pair interaction potential for two molecules with long axes \mathbf{a}_1 and \mathbf{a}_2 located at points 1 and 2, respectively, while \mathbf{n}_1 is the director at point 1 and \mathbf{n}_2 is the director at point 2. The first term in Eq. (5) is the entropy, the second term is the internal energy, and the third term is the energy of interaction of molecular longitudinal dipoles with electric field. At any point \mathbf{r} , the orientational distribution function $f[(\mathbf{a} \cdot \mathbf{n}), \mathbf{r}]$ in Eq. (5) satisfies the normalizing constraint:

$$\int d^2 \mathbf{a} f[(\mathbf{a} \cdot \mathbf{n}(\mathbf{r})), \mathbf{r}] = 1 \quad . \quad (6)$$

Minimizing the free energy (5) with respect to orientational distribution function $f[(\mathbf{a} \cdot \mathbf{n}), \mathbf{r}]$ under constraint (6), one obtains:

$$f[(\mathbf{a} \cdot \mathbf{n}), \mathbf{r}] = \frac{1}{I_0(\mathbf{r})} \exp \left\{ - \frac{U_{MF+E}[(\mathbf{a} \cdot \mathbf{n}), \mathbf{r}]}{k_B T} \right\} \quad , \quad (7)$$

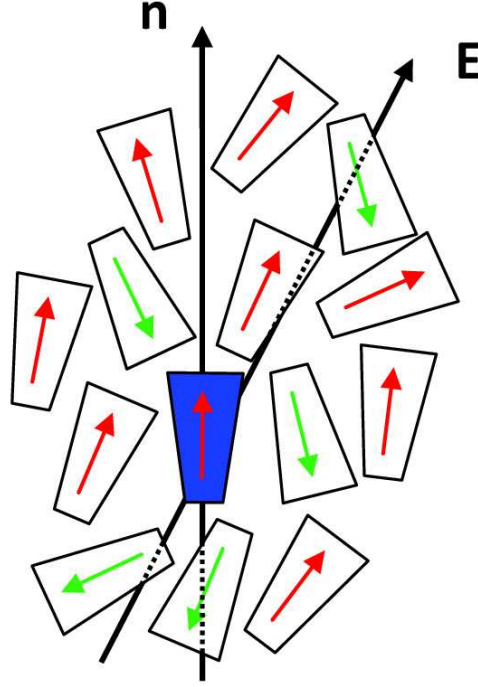


FIG. 9: A trial (blue) polar molecule in a combination of the mean molecular field and electric field \mathbf{E} . Here \mathbf{n} is the local director at a point, where trial molecule is located.

where $\mathbf{r} \equiv \mathbf{r}_1$, $\mathbf{n} \equiv \mathbf{n}_1$, $I_0(\mathbf{r})$ is the normalizing constant, and $U_{MF+E}[(\mathbf{a} \cdot \mathbf{n}), \mathbf{r}]$ is the potential of a molecule located at point \mathbf{r} with orientation $\mathbf{a} \equiv \mathbf{a}_1$ of prime axis in a combination of the mean molecular field and electric field:

$$U_{MF+E}[(\mathbf{a} \cdot \mathbf{n}), \mathbf{r}] \equiv \frac{\sigma_0}{4\pi V_0} \int d^3 \mathbf{r}_{12} \int d^2 \mathbf{a}_2 f[(\mathbf{a}_2 \cdot \mathbf{n}_2), \mathbf{r}_2] \left[U_{12}^{ef}(\mathbf{a}_1, \mathbf{a}_2, \mathbf{r}_{12}) - \mu(\mathbf{a} \cdot \mathbf{n})(\mathbf{n} \cdot \mathbf{E}) \right] . \quad (8)$$

Approximating the pair potential by spherical invariants [Eq. (1)], substituting Eq. (1) into Eq. (8), introducing coefficients

$$J_{\ell L \lambda}^{(i)} \equiv \frac{\sigma_0}{4\pi V_0} \int_0^\infty dr_{12} r_{12}^{i+2} J_{\ell L \lambda}(r_{12}) \quad (9)$$

and using only T_{101} , T_{110} , T_{011} and T_{202} spherical invariants resulting in average in the appearance of the terms in the mean field depending on the powers of operator ∇ not higher than one, one finally obtains the following expression for the potential of a molecule with orientation \mathbf{a} affected by a combination of the mean molecular field and electric field:

$$-U_{MF+E}(t, \mathbf{r}) = J_{101}^{(0)} P(\mathbf{r}) P_1(t) + J_{202}^{(0)} S(\mathbf{r}) P_2(t) + \left\{ \frac{1}{6} \left[J_{110}^{(1)} + J_{011}^{(1)} \right] (\nabla \cdot \mathbf{n}) + \mu(\mathbf{n} \cdot \mathbf{E}) \right\} P_1(t) , \quad (10)$$

where $t \equiv (\mathbf{a} \cdot \mathbf{n})$, $P_1(t) \equiv t$ and $P_2(t) \equiv 3/2 t^2 - 1/2$ are the first and the second Legendre polynomials. Eq. (10) corresponds to the first (simplest) approximation reflecting modulation of the S and P order parameters caused by modulation of splay and describing the major tendency: both parameters S and P should be higher (lower) at the places where the splay is higher (lower). The first two terms in Eq. (10) are the polar and non-polar anisotropies, while the two terms in figure brackets are due to the flexoelectric effect and electric field. From Eqs. (2), (7) and (10) one readily obtains the following recurrent equations for determination of the $P(\mathbf{r})$ and $S(\mathbf{r})$ order parameters at each temperature T and electric field E at any given $\mathbf{n}(\mathbf{r})$ distribution:

$$P(\mathbf{r}) = \frac{I_1(\mathbf{r})}{I_0(\mathbf{r})} , \quad S(\mathbf{r}) = \frac{I_2(\mathbf{r})}{I_0(\mathbf{r})} , \quad (11)$$

where integrals $I_m(\mathbf{r})$ are defined as follows:

$$I_m(\mathbf{r}) \equiv \int_{-1}^1 P_m(t) \exp\left\{-\frac{U_{MF+E}(t, \mathbf{r})}{k_B T}\right\} dt \quad , \quad (12)$$

where U_{MF+E} is determined by Eq. (10). Substituting solution (7)–(10) back into Eq. (5), one obtains for the equilibrium free-energy density $\partial F_{\text{eq}}/\partial V$:

$$4\pi V_0 \frac{\partial F_{\text{eq}}(\mathbf{r})}{\partial V} = -k_B T \ln I_0(\mathbf{r}) + \frac{1}{2} J_{101}^{(0)} P^2(\mathbf{r}) + \frac{1}{2} J_{202}^{(0)} S^2(\mathbf{r}), \quad (13)$$

where normalizing integral $I_0(\mathbf{r})$ should be calculated using Eqs. (12) and (10). Eq. (13) should be used for comparison of the free energies of the neighboring phases in the phase diagram.

As it was mentioned in Sec. II, Eq. (4) [multiplied by $4\pi V_0$] is the explicitly depending on director \mathbf{n} part of Eq. (5). Indeed, if one prolongs the gradient expansion in Eq. (10) up to the terms depending on the second power of operator ∇ (for this purpose, invariants T_{220} , T_{022} , T_{222} , T_{422} and T_{224} should also be considered in approximation Eq. (1); this is done in Ref.[43]) and substitutes Eq. (10) into the second and third terms of Eq. (5) [definition Eq. (8) should also be used], then one obtains Eq. (4). In particular, the flexoelectric and electric-field-dependent terms (which explicitly depend on both P and \mathbf{n}) coincide in Eqs. (4) and (5) at substitution of $4\pi V_0 K_{11} \lambda = [J_{110}^{(1)} + J_{011}^{(1)}]/6$ and $V_0 \varepsilon_a = \mu(\sigma_0 + 1)$. By the same substitution of Eq (10) into Eq. (5), one obtains the P^2 term introduced phenomenologically in Ref. [35]. In the same manner, it is possible to obtain additional contributions to the elastic constants depending on the polar order parameter P studied phenomenologically in Refs. [18, 35] (see also Ref. [32]).

B. Perturbation elastic continuum theory reflecting space variation of S and P order parameters

Let us now consider the director distribution in the polar phases in the presence of electric field, having in mind the results obtained in Sec. IV A. In the cases presented in Figs. 2 (a) and (b), we expect that director is (mostly) along the radial planes (the planes parallel to the cylinder axis \mathbf{x} and radius \mathbf{r}). Thus, in all cases presented in Fig. 2, the director mainly has two nonzero coordinates, similarly to that in Ref. [46]:

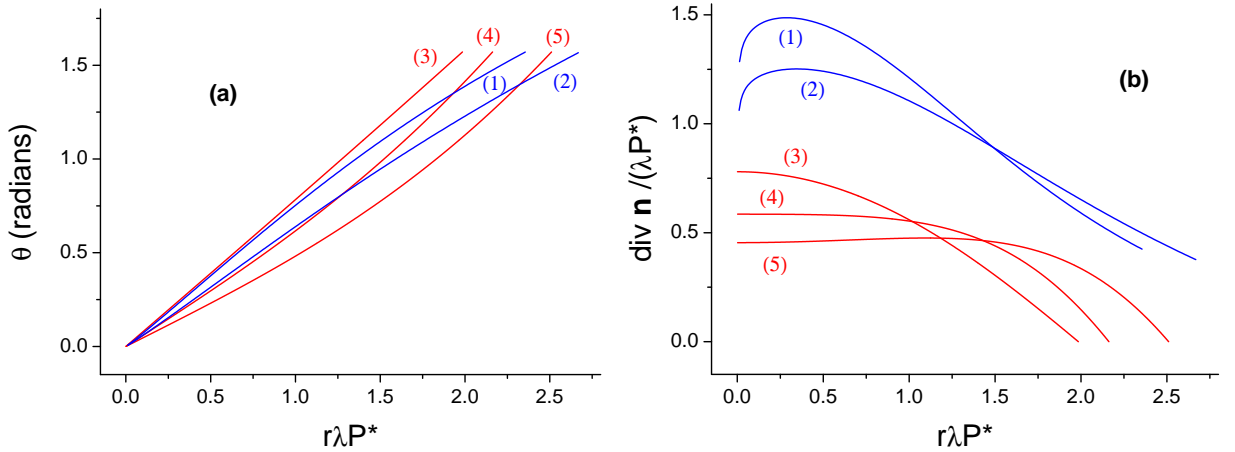


FIG. 10: Tilt of director (a) and splay deformation (b) distributions within the domain in N_F^{2D} [blue curves (1) and (2)] and N_F^{1D} [red curves (3), (4) and (5)]. Here $\tilde{\tau} = 0.001$ (1), 0.22 (2), 0.225 (3), 0.8 (4) and 0.843 (5).

$$n_x = \cos \theta(r) \quad , \quad n_r = \sin \theta(r) \quad . \quad (14)$$

One notes, that all the structures presented in Fig. 2 can be described in a unified way, and here we also introduce the δ parameter to distinguish between the double- and single-splay structures (δ is set to one in the case of 2D-splay and is set to zero in the case of 1D-splay). From Eq. (14) it follows:

$$(\nabla \cdot \mathbf{n}) = \frac{\delta}{r} \sin \theta + \cos \theta \frac{d\theta}{dr} \quad , \quad [\mathbf{n} \times [\nabla \times \mathbf{n}]]^2 = \sin^2 \theta \left(\frac{d\theta}{dr} \right)^2 \quad . \quad (15)$$

In the manner of paper [32], let us consider the one-constant approximation $K_{11} = K_{33} \equiv K$ for simplicity. An equilibrium director $\mathbf{n}(\mathbf{r})$ distribution should be obtained by independent minimization of free-energy density (4), while an equilibrium polarization $P(\mathbf{r})$ distribution has already been obtained by independent minimization of free-energy density (5) and is presented by Eq. (11). Precise minimization of Eq. (4) with constraint (11) appears to

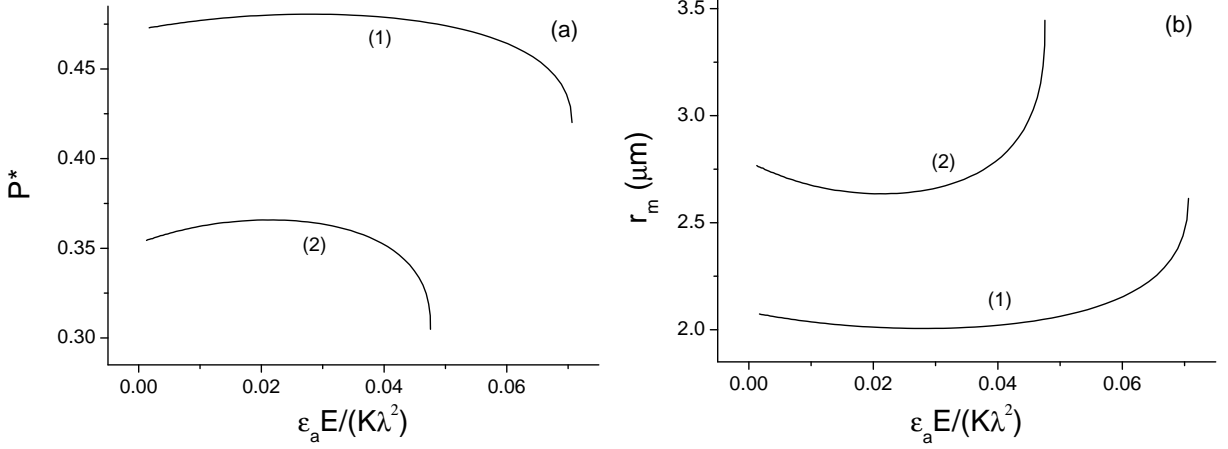


FIG. 11: Electric field dependencies of the characteristic polar order parameter (a) and domain radius (b) in N_F^{1D} at $\sigma_0 J_{202}^{(0)} / k_B = 2032 K$, $\sigma_0 J_{101}^{(0)} / k_B = 362 K$, $\lambda = 2 \mu\text{m}^{-1}$, $J_A / k_B = 113 K \mu\text{m}$, $K V_0 = 5 \times 10^{-35} N m^3$ and $T = 70^\circ\text{C}$ [curves (1)] and 81°C [curves (2)].

be complicated. The complexity is in the fact that minimization with respect to director \mathbf{n} and polarization value P should be done independently, while varying in the space polarization P (and this variation is unknown before we know the distribution of \mathbf{n}) participates in differential Eq. (4), from where this distribution of \mathbf{n} is supposed to be obtained. For this purpose, let us consider a perturbation theory based on the assumption that variation of the order parameters in space is small. In the framework of perturbation theory, let us first consider the uniform polarization $P(\mathbf{r}) = P^*$ in Eq. (4). In both cases of ferroelectric domains presented in Figs. 3 (b) and (c), let us consider variation of angle θ from zero (at the \mathbf{x} -axis of one domain) to π (at the \mathbf{x} -axis of the neighboring domain). Then the same simplification for the free-energy density is valid for all the structures presented in Fig. 2: all the terms proportional either to $d\theta/dr$ or to λ should have opposite signs in the neighboring domains, and the corresponding terms vanish in average. Taking this into account, substituting Eq. (15) into Eq. (4), and minimizing free-energy density (4) with respect to θ and $d\theta/dr$, as presented, for example, in Ref. [47], Appendix A, one obtains the following equation of state:

$$\left(\frac{d\theta}{dr}\right)^2 + \tau^2 |\cos \theta| - \frac{\delta}{r^2} \sin^2 \theta = \frac{\tau^2}{k^2} \quad , \quad (16)$$

where $\tau \equiv \sqrt{2\varepsilon_a E P^* / K}$ is the reduced electric field, and k is some constant independent of angle θ , which should be obtained by independent minimization of the free-energy density. Introducing new dimensionless variable $\psi \equiv \tau r / k$, one obtains from Eq. (16):

$$\frac{d\theta}{d\psi} = \sqrt{1 - k^2 |\cos \theta| + \delta / \psi^2 \sin^2 \theta} \quad . \quad (17)$$

Radius r_m of the domain can now be found by minimization of the free energy with respect to parameter k . This, however, can be done in a more precise way partially taking into account the non-uniformity of $P(\mathbf{r})$. Indeed, from Eq. (11) it approximately follows [after expansion of the exponent in Eq. (12) in Taylor series with substitution of Eq. (10)] that $P(\mathbf{r}) \sim (\nabla \cdot \mathbf{n}) + \varepsilon_a E \cos \theta / (K\lambda)$, where the first term is flexoelectric polarization and the second term is induced by electric field polarization. One notes from Eq. (4) that any re-scale of coordinate r , at which $r\lambda P$ and $\tau / (\lambda P)$ remain constant, does not change the free-energy density. This means in the end that distribution of polarization is determined only by distribution of angle θ in the space. Let us therefore write the following trial approximation for the polar order parameter:

$$P(\theta) = P^* r_m \{(\nabla \cdot \mathbf{n}) + \tau^2 \cos \theta / (2\lambda P^*)\} = P^* \psi_m \left\{ \frac{\delta}{\psi} \sin \theta + \cos \theta \left(\frac{d\theta}{d\psi} + \frac{1}{2} k \tilde{\tau} \right) \right\} \quad . \quad (18)$$

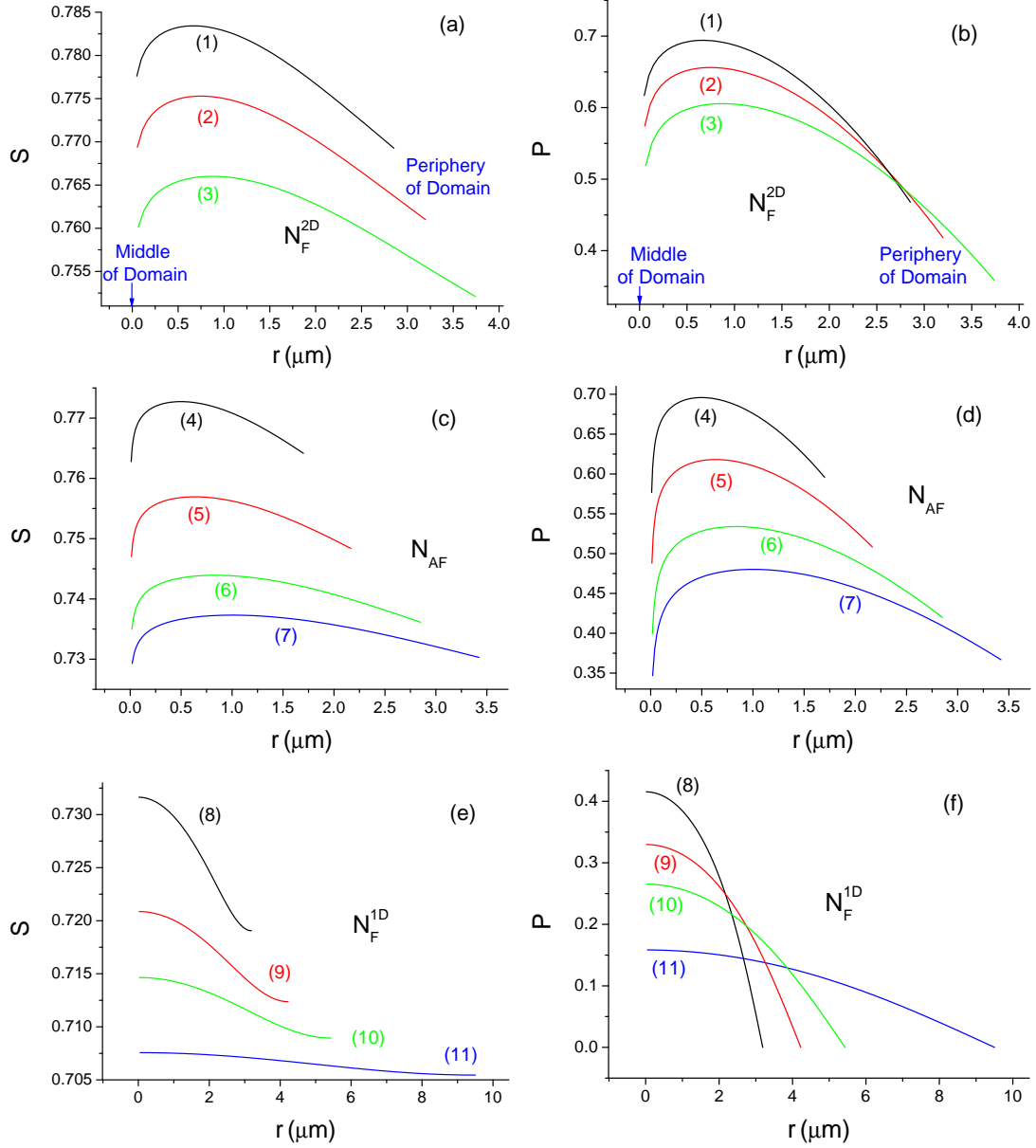


FIG. 12: Distribution of the S [(a),(c),(e)] and P [(b),(d),(f)] orientational order parameters within the domains in N_F^{2D} [(a),(b)], N_{AF} [(c),(d)] and N_F^{1D} [(e),(f)] at $T = 57^\circ\text{C}$ (1); 62°C (2); 67°C (3); 69°C (4); 76°C (5); 81°C (6); 83°C (7); 85°C (8); 88°C (9); 90°C (10); 92°C (11) at $E = 0$, $\sigma_0 J_{202}^{(0)}/k_B = 2032\text{ K}$, $\sigma_0 J_{101}^{(0)}/k_B = 362\text{ K}$, $\lambda = 2\mu\text{m}^{-1}$, $J_A/k_B = 113\text{ K}\mu\text{m}$ and $K V_0 = 5 \times 10^{-35}\text{ N m}^3$. Radius r is defined in Fig. 2 for all the polar phases.

One notes from Eq. (18) that, in the case of N_F^{2D} , the P^* proportionality coefficient coincides with P at $\theta = \pi/2$ (polar order parameter at periphery r_m of ferroelectric domain). In the cases of N_F^{2D} and N_{AF} , the P^* coefficient formally corresponds to different place r^* within the domain, other than periphery r_m . Regardless of the kind of the domain, however, the expression in figure brackets in Eq. (18) is equal to $1/r_m$ at r^* . Substituting Eqs. (15), (17) and (18) into Eq. (4), integrating the free-energy density along the radius of domain (with the $r dr$ Jacobian for 2D-splay or with the dr Jacobian for 1D-splay) and dividing the result by the cross section area (for 2D-splay) or by the length of domain (for 1D-splay), one obtains the expression for the average free-energy density, which should be farther minimized with parameter k . This could be done for each polar nematic phase similarly to that presented in Ref. [32] for N_{AF} . Subsequently, at any value of $\tilde{\tau}$, the $r(\theta)$ dependence can be obtained, and, in particular, radius r_m of the domain can be obtained. In N_{AF} , $r_m \lambda P^* \approx 1.55$ and maximum tilt is $\theta_m \approx 64^\circ$. In N_F^{1D} and N_F^{2D} , radius r_m of the domain generally depends on the applied electric field, while maximum tilt is always equal

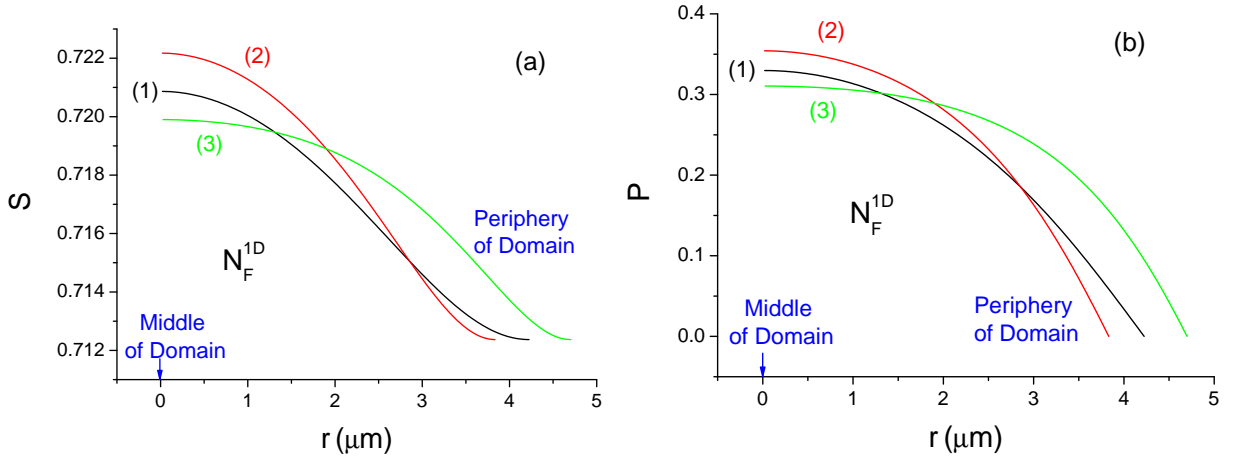


FIG. 13: Distribution of the S (a) and P (b) orientational order parameters within the domains in N_F^{1D} at $\varepsilon_a E / (K \lambda^2) = 0$ (1); 0.01 (2); 0.028 (3) at $T = 87^\circ\text{C}$, $\sigma_0 J_{202}^{(0)} / k_B = 2032\text{ K}$, $\sigma_0 J_{101}^{(0)} / k_B = 362\text{ K}$, $\lambda = 2\ \mu\text{m}^{-1}$, $J_A / k_B = 113\text{ K}\mu\text{m}$ and $K V_0 = 5 \times 10^{-35}\text{ N m}^3$. Radius r is defined in Fig. 2 (c).

to $\theta = \pi/2$. Several $\theta(r)$ and $(\nabla \cdot \mathbf{n})$ dependencies at several particular values of dimensionless electric field $\tilde{\tau}$ are presented in Figs. 10 (a) and (b), respectively, for N_F^{2D} [blue curves (1) and (2)] and N_F^{1D} [red curves (3), (4) and (5)]. One notes that the tilt of director varies almost linearly in both N_F^{2D} and N_F^{1D} , with a slight tendency to greater variation in the middle of each domain in N_F^{2D} and, oppositely, at the domain periphery ($r = r_m$) in N_F^{1D} . From Fig. 10 it follows that, at moderate values of electric field, the maximum splay deformation in N_F^{1D} is achieved at $\theta = 0$, at which the director is parallel to electric field. This is the configuration, at which both flexoelectric and induced polarizations give optimal summarized contribution to the free energy. Therefore both N_F^{2D} and N_{AF} exhibit a transition into N_F^{1D} at application of electric field. However, there always exists a disbalance between the induced and flexoelectric polarizations. Indeed, the flexopolarization can exist only in the presence of director deformation. However, at application of electric field, the structure becomes more uniform, and the splay deformation reduces. Therefore, at higher electric field, the maximum in Fig. 10 (b) reduces and shifts to the position, where director is not parallel to electric field. At $\tilde{\tau} \approx 0.843$, the splay phase becomes unstable, and a transition into paraelectric nematic phase happens. The electric field dependencies of characteristic polar order parameter P^* and domain radius r_m at particular fixed temperatures within N_F^{1D} are presented in Figs. 11 (a) and (b), respectively. Both dependencies are generally not monotonic because of the nontrivial correlation between splay and electric field. At higher value of electric field, P^* greatly decreases and r_m greatly increases just before the transition into N .

Knowing the director distribution in space in N_F^{2D} , N_{AF} and N_F^{1D} , one obtains the distributions of S and P order parameters in each phase using Eqs. (10)–(12). For this purpose, one should substitute approximation (18) into Eq. (10). In particular, at specific places r^* within each domain, where polar order parameter P coincides with coefficient P^* , one immediately obtains that the whole expression in figure brackets in Eq. (10) is equal to $[J_{110}^{(1)} + J_{011}^{(1)}] / (6r_m)$. From recurrent Eqs. (11)–(12) one obtains S^* and P^* first, and then the whole distribution of $S(r)$ and $P(r)$ within the domain, which are presented in Fig. 12. One notes that both S and P generally decrease with the increasing temperature. The maximal values of both parameters are observed close to the middle of domain in N_F^{2D} and N_{AF} and in the middle exactly in N_F^{1D} . Polar order parameter reaches zero at the periphery of each domain in N_F^{1D} , while in N_F^{2D} and N_{AF} it does not, which means that flexopolarization exhibits step-wise reversal between the domains without director disruption. Distributions of $S(r)$ and $P(r)$ at several non-zero values of electric field are also presented in Fig. 13. One notes that profiles of both S and P first tend to become sharper at moderate electric field and then smoother at higher electric field.

C. Computer simulations

To perform calculations of director distribution in a polar nematic film under the action of electric field, we have modified the existing extended Frank elastic continuum approach [32], previously used for calculations of polar nematic material. The original approach takes into account the effects of director field distortion with the $\lambda(\mathbf{n} \cdot \mathbf{p})$ term included, as well as the formation of defects and finite energy of the surface boundaries. In this paper, we have modified the

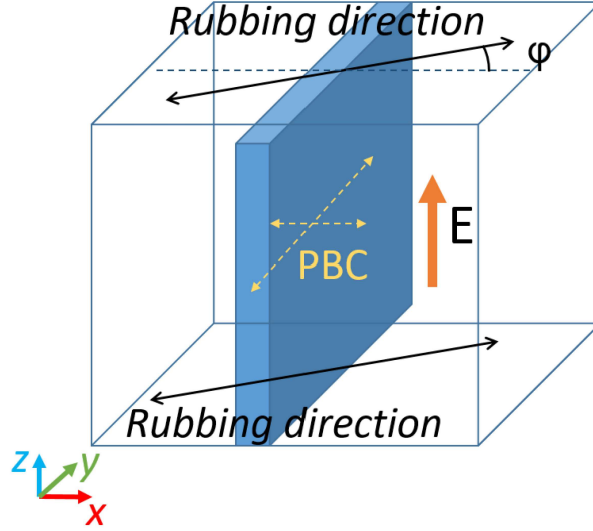


FIG. 14: Principal geometry of the simulations box and the polar nematic film. Black arrows show the rubbing direction of planar alignment of the film. Orange arrow shows the electric field direction. Yellow dash arrows show the periodic boundary condition directions of the simulation box.

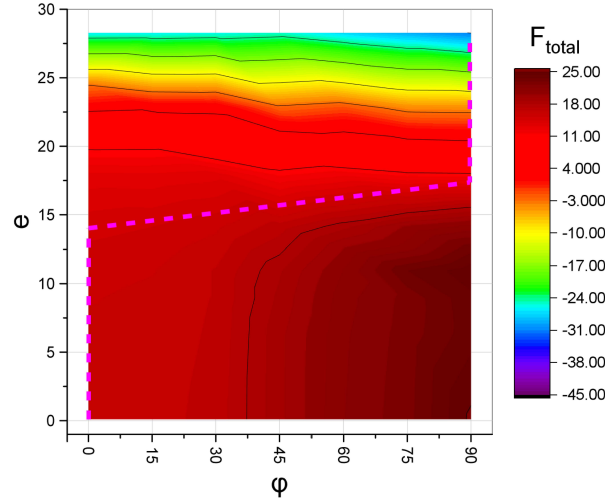


FIG. 15: Dependence of the total free energy on the value of dimensionless electric field e and rubbing direction orientation φ . Violet dash line traces energy minimum over e .

free energy to take into account the action of an electric field:

$$F = \frac{1}{2} \int_V \left\{ K_{11}(\mathbf{n} \cdot \nabla \cdot \mathbf{n}) - \lambda \mathbf{p} \right\}^2 + K_{22}(\mathbf{n} \cdot [\nabla \times \mathbf{n}])^2 + K_{33}[\mathbf{n} \times [\nabla \times \mathbf{n}]]^2 \right\} dV - \varepsilon_a \int_V (\mathbf{n} \cdot \mathbf{p})(\mathbf{n} \cdot \mathbf{E}) dV + \frac{W}{2} \int_{\Omega} (1 - \cos^2 \gamma) d\Omega + F_{\text{def}} \quad , \quad (19)$$

where K_{11} , K_{22} and K_{33} are the splay, twist and bend elastic constants, respectively, $K_{11}\lambda$ is the flexoelectric constant, \mathbf{p} is polarizability direction vector, \mathbf{E} is electric field intensity, V is the bulk of the sample having surface Ω , W is the surface anchoring energy density, γ is the angle between local director and normal to the surface, F_{def} is the energy of defects calculated by the summation of the point and linear defect energies (see the details in Ref. [48]). The details of optimization are presented in Ref. [32]. For simplicity, polarizability direction vector \mathbf{p} is supposed to be a unit vector parallel or anti-parallel to \mathbf{n} in each point. In addition, in correspondence with theoretical part of the paper, an algorithm accepted only those steps with $(\mathbf{n} \cdot \mathbf{p})(\mathbf{n} \cdot \mathbf{E}) \geq 0$. As a result, our simulation annealing procedure leads

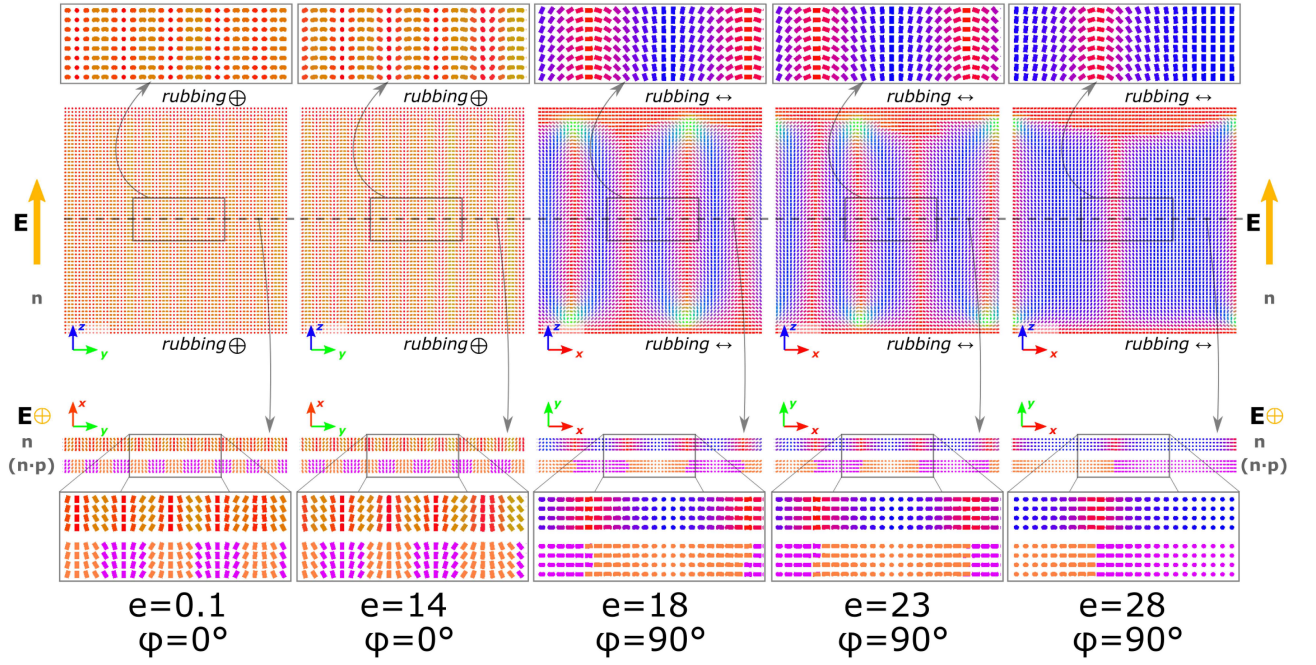


FIG. 16: Director \mathbf{n} and polarizability $(\mathbf{n} \cdot \mathbf{p})$ distributions at various dimensionless electric field e values in the central cross-cuts perpendicular to the film plane (top) and along the film plane (bottom). Director distributions are shown in color, corresponding to the direction of \mathbf{n} (x - red, y - green, z - blue). Polarizability is shown in orange $[(\mathbf{n} \cdot \mathbf{p}) = 1]$ and violet $[(\mathbf{n} \cdot \mathbf{p}) = -1]$.

to minimization of the free energy over both director \mathbf{n} and polarizability direction \mathbf{p} distributions in a self-consistent way.

The one-constant approximation was used for simplicity: $K_{11} : K_{22} : K_{33} = 1 : 1 : 1$, and the value of λ is set to 10. To take into account the potential formation of disclination lines, their cores linear energy density was set to $f_{core}^{line} = 10K_{11}$. The cubic simulation box of size $0.125 \times 2 \times 2$ was rendered into $4 \times 64 \times 64$ lattice. For x and y facets, the periodic boundary conditions were applied. For z facet, planar aligned boundary conditions were set with rubbing direction having angle $\varphi \in [0^\circ; 90^\circ]$ with the x axis and $\mu_1 = Wd/K_{11} = 400$, where d is the film thickness (see Fig. 14). The electric field \mathbf{E} was oriented perpendicular to the film plane, and the value of dimensionless electric field intensity $e = Ed(\frac{\epsilon_0}{K_{11}})^{1/2}$ varied from 0.1 to 30. For each e , we produced 6.1×10^{10} steps (3×10^7 parallel multisteps) Monte-Carlo annealing optimization with 4 independent runs to find the energy-optimal structures.

The resulting structures strongly depend on the value of electric field and the rubbing direction φ . Fig. 15 shows the dependency of the total free energy of the system on these two parameters. At low value of electric field (e from 0.1 to 14), the energy-optimal structure corresponds to the antiferroelectric splay in the xy plane (supposed to be the plane of the substrate in real experiment) with alternating sign of polarizability. The average director orientation is almost parallel to the rubbing direction. Some slight ferroelectric modulation is also present: a projection of director along electric field arises in the middle of each antiferroelectric domain, so that the projection of director lines on the zy plane (perpendicular to rubbing) gains the shape of periodical arcs. This structure is visualized as longitudinal to the rubbing direction stripes (Fig. 16). Above the threshold value $e^* \approx 15$, the system undergoes a transition related to the reorientation of the arcs along the rubbing direction, and the arcs themselves become much bigger, while the antiferroelectric modulation in the xy plane disappears. This structure (at $e > 15$) is visualized as transverse to the rubbing direction stripes (Fig. 16). At further increasing electric field, the layer period starts growing [similarly to that in theory, see Fig. 11 (b)], and the director divergence in the middle each domain decreases [similarly to that in theory, see Fig. 10 (b)]. Computer simulations describe well the transformation from antiferroelectric to ferroelectric structure with the reorientation of stripes, which is observed experimentally and presented in Sec. III A.

V. CONCLUSION

The origin and structures of ferroelectric and antiferroelectric splay nematic phases are outlined. The double-splay ferroelectric N_F^{2D} and antiferroelectric N_{AF} nematic phases are composed of quasi-cylindrical periodical domains.

Without electric field, N_F^{2D} and N_{AF} are observed in the lower-temperature range. The single-splay ferroelectric N_F^{1D} nematic phase is composed of planar periodical domains. Without electric field, N_F^{1D} is observed in the higher-temperature range. In the presence of electric field, all the splay nematic phases first (at moderate electric field) transform into N_F^{1D} and then (at higher electric field) – into paraelectric nematic phase N having uniform director orientation. The origin of all the splay nematic phases is flexoelectric effect due to the polarity of molecules. The origin of the transformations between phases in electric field is the non-trivial interplay between flexoelectric and induced polarizations. The distribution of director and both polar P and non-polar S orientational order parameters within the domains of all the splay nematic phases is found. Variation of the structure and properties of the splay nematic phases with variation of temperature and electric field are investigated. The electric field – temperature phase diagram is obtained. The equilibrium domain size was found to increase and polarization was found to decrease in each polar phase with the increasing temperature. Several additional phase transitions related to optimization of the domains within the cell gap were found and explained.

Acknowledgments

A.V.E. and V.Yu.R. thank the Russian Foundation for Basic Research (project No. 21-53-50008) for the financial support of theoretical investigation presented in this work. F.A, H.N and K.I. thank Japan Society for the Promotion of Science (project No. JPJSBP120214814) for the financial support of experimental investigation presented in this work. The research was carried out using the equipment of the shared research facilities of HPC computing resources at Lomonosov Moscow State University. The authors are grateful to S.A. Shvetsov for help.

-
- [1] R. J. Mandle, *Soft Matter* **18**, 5014 (2022). DOI: 10.1039/D2SM00543C
- [2] A. G. Vanakaras and D. J. Photinos, *Mol. Cryst. Liq. Cryst.* **395**, 213 (2003). DOI: 10.1080/15421400390193783
- [3] H. Takezoe, *Ferroelectrics* **468**, 1 (2014). DOI: 10.1080/00150193.2014.932653
- [4] H. Takezoe, *Mol. Cryst. Liq. Cryst.* **646**, 46 (2017). DOI:10.1080/15421406.2017.1284377
- [5] F. Vita, F. C. Adamo, and O. Francescangeli, *J. Mol. Liq.* **267**, 564 (2018). DOI: 10.1016/j.molliq.2018.02.084
- [6] O. Francescangeli and E. T. Samulski, *Soft Matter* **6**, 2413 (2010). DOI: 10.1039/C003310C
- [7] E. Gorecka, D. Pocięcha, J. Mieczkowski, J. Matraszek, D. Guillon, and B. Donnio, *J. Am. Chem. Soc.* **126**, 15946 (2004). DOI: 10.1021/ja044597k
- [8] C. F. C. Fitie, W. S. C. Roelofs, M. Kemerink, and R. P. Sijbesma, *J. Am. Chem. Soc.* **132**, 6892 (2010). DOI: 10.1021/ja101734g
- [9] D. Miyajima, F. Araoka, H. Takezoe, J. Kim, K. Kato, M. Takata, and T. Aida, *Science* **336**, 209 (2012). DOI: 10.1126/science.1219171
- [10] V. Novotna, M. Glogarova, V. Hamplova, and M. Kaspar, *J. Chem. Phys.* **115**, 9036 (2001). DOI: 10.1063/1.1412871
- [11] D. Catalano, V. Domenici, A. Marini, C. A. Veracini, A. Bubnov, and M. Glogarova, *J. Phys. Chem. B* **110**, 16459 (2006). DOI: 10.1021/jp0621777
- [12] A. Bubnov, V. Novotna, V. Hamplova, M. Kaspar, and M. Glogarova, *J. Mol. Struct.* **892**, 151 (2008). DOI: 10.1016/j.molstruc.2008.05.016
- [13] Y. Na, Y. Naruse, N. Fukuda, H. Orihara, A. Fajar, V. Hamplova, M. Kaspar, and M. Glogarova, *Ferroelectrics* **364**, 13 (2008). DOI: 10.1080/00150190802046703
- [14] A. V. Emelyanenko, *Crystals* **9**, 583 (2019). DOI: 10.3390/cryst9110583
- [15] H. Nishikawa, K. Shiroshita, H. Higuchi, Y. Okumura, Y. Haseba, S. Yamamoto, K. Sago, and H. Kikuchi, *Adv. Mater.* **29**, 1702354 (2017). DOI: 10.1002/adma.201702354
- [16] R. J. Mandle, S. J. Cowling, and J. W. Goodby, *Chem. Eur. J.* **23**, 14554 (2017). DOI: 10.1002/chem.201702742
- [17] R. J. Mandle, S. J. Cowling, and J. W. Goodby, *Phys. Chem. Chem. Phys.* **19**, 11429 (2017). DOI: 10.1039/C7CP00456G
- [18] A. Mertelj, L. Cmok, N. Sebastian, R. J. Mandle, R. R. Parker, A. C. Whitwood, J. W. Goodby, and M. Copic, *Phys. Rev. X* **8**, 041025 (2018). DOI: 10.1103/PhysRevX.8.041025
- [19] R. J. Mandle and A. Mertelj, *Phys. Chem. Chem. Phys.* **21**, 18769 (2019). DOI: 10.1039/C9CP03581H
- [20] S. Dhakal and J. V. Selinger, *Phys. Rev. E* **81**, 031704 (2010). DOI: 10.1103/PhysRevE.81.031704
- [21] R. J. Mandle, N. Sebastian, J. Martinez-Perdiguero and A. Mertelj, *Nat. Comm.* **12**, 4962 (2021). DOI: 10.1038/s41467-021-25231-0
- [22] R. J. Mandle, S. J. Cowling and J. W. Goodby, *Liq. Cryst.* **48**, 1780 (2021). DOI: 10.1080/02678292.2021.1934740
- [23] E. Cruickshank, R. Walker, J. M. D. Storey and C. T. Imrie, *RSC Adv.* **12**, 29482 (2022). DOI: 10.1039/d2ra05628c
- [24] J. Li, Z. Wang, M. Deng, Y. Zhu, X. Zhang, R. Xia, Y. Song, Y. Hisai, S. Aya and M. Huang, *Giant* **11**, 100109 (2022). DOI: 10.1016/j.giant.2022.100109
- [25] R. J. Mandle, *Liq. Cryst.* **49**, 2019 (2022). DOI: 10.1080/02678292.2022.2145380

- [26] S. Brown, E. Cruickshank, J. M. D. Storey, C. T. Imrie, D. Pocięcha, M. Majewska, A. Makal, and E. Gorecka, *Chem. Phys. Chem.* **22**, 1 (2021). DOI: 10.1002/cphc.202100644
- [27] J. Li, H. Nishikawa, J. Kougo, J. Zhou, S. Dai, W. Tang, X. Zhao, Y. Hisai, M. Huang, and S. Aya, *Sci. Adv.* **7**, (2021). DOI: 10.1126/sciadv.abf5047
- [28] N. Sebastian, M. Copic, and A. Mertelj, *Phys. Rev. E* **106**, 021001 (2022). DOI: 10.1103/PhysRevE.106.021001
- [29] J. Ortega, C. L. Folcia, J. Etxebarria, *Liq. Cryst.* **49**, 2128 (2022). DOI: 10.1080/02678292.2022.2104949
- [30] H. Nishikawa and F. Araoka, *Adv. Mater.* **33**, 2101305 (2021). DOI: 10.1002/adma.202170270
- [31] X. Zhao, J. Zhou, J. Li, J. Kougo, Z. Wan, M. Huang, and S. Aya, *Proc. Natl. Acad. Sci.* **118**, e2111101118 (2021). DOI: 10.1073/pnas.2111101118
- [32] A. V. Emelyanenko, V. Yu. Rudyak, S. A. Shvetsov, F. Araoka, H. Nishikawa, and K. Ishikawa, *Phys. Rev. E* **105**, 064701 (2022). DOI: 10.1103/PhysRevE.105.064701
- [33] M. P. Rosseto and J. V. Selinger, *Phys. Rev. E* **101**, 052707 (2020). DOI: 10.1103/PhysRevE.101.052707
- [34] J. V. Selinger, *Annu. Rev. Condens. Matter Phys.* **13**, 49 (2022). DOI: 10.1146/annurev-conmatphys-031620-105712
- [35] N. Sebastian, L. Cmok, R. J. Mandle, M. R. de la Fuente, I. Drevensek Olenik, M. Copic, and A. Mertelj, *Phys. Rev. Lett.* **124**, 037801 (2020). DOI: 10.1103/PhysRevLett.124.037801
- [36] N. Sebastian, M. Lovsin, B. Berteloot, N. Osterman, A. Petelin, R. J. Mandle, S. Aya, M. Huang, I. Drevensek-Olenik, K. Neyts and A. Mertelj, *Nature Communications* **14**, 3029 (2023). DOI: 10.1038/s41467-023-38749-2
- [37] M. T. Mathe, B. Farkas, L. Peter, A. Buka, A. Jakli and P. Salamon, *Scientific Reports* **13**, 6981 (2023). DOI: 10.1038/s41598-023-34067-1
- [38] C. L. Folcia, J. Ortega, R. Vidal, T. Sierra and J. Etxebarria, *Liq. Cryst.* **49** 899 (2022). DOI: 10.1080/02678292.2022.2056927
- [39] K. Perera, R. Saha, P. Nepal, R. Dharmarathna, M. S. Hossain, M. Mostafa, A. Adaka, R. Waroquet, R. J. Twieg and A. Jakli, *Soft Matter* **19**, 347 (2023). DOI: 10.1039/D2SM01395A
- [40] A. Sterle, L. Cmok, N. Sebastian, A. Mertelj, Y. Kong, X. Zhang, I. Drevensek-Olenik, *OME* **13**, 282 (2023). DOI: 10.1364/OME.477717
- [41] J. Yang, Y. Zou, W. Tang, J. Li, M. Huang and S. Aya, *Nature Communications* **13**, 7806 (2022). DOI: 10.1038/s41467-022-35443-7
- [42] R. Saha, P. Nepal, C. Feng, M. S. Hossein, J. T. Gleeson, S. Sprunt, R. J. Twieg and A. Jakli, *Liq. Cryst.* **49**, 1784 (2022). DOI: 10.1080/02678292.2022.2069297
- [43] A. V. Emelyanenko, E. S. Filimonova, and A. R. Khokhlov, *Phys. Rev. E* **103**, 022709 (2021). DOI: 10.1103/PhysRevE.103.022709
- [44] A. V. Emelyanenko and A. R. Khokhlov, *J. Chem. Phys.* **142**, 204905 (2015). DOI: 10.1063/1.4921684
- [45] N. Sebastian, R. J. Mandle, A. Petelin, A. Eremin and A. Mertelj, *Liq. Cryst.* **48** 2055 (2021). DOI: 10.1080/02678292.2021.1955417
- [46] Yu. Garbovskiy, A. V. Emelyanenko and A. Glushchenko, *Nanoscale* **12**, 16438 (2020). DOI: 10.1039/D0NR05301E
- [47] A. V. Emelyanenko, *Phys. Rev. E* **82**, 031710 (2010). DOI: 10.1103/PhysRevE.82.031710
- [48] V. Yu. Rudyak, A. V. Emelyanenko, and V. A. Loiko, *Phys. Rev. E* **88**, 052501 (2013). DOI: 10.1103/PhysRevE.88.052501